



## **Beating Crystallization in Glass-Forming Metals by Millisecond Heating and Processing**

William L. Johnson, et al. Science **332**, 828 (2011); DOI: 10.1126/science.1201362

This copy is for your personal, non-commercial use only.

If you wish to distribute this article to others, you can order high-quality copies for your colleagues, clients, or customers by clicking here.

**Permission to republish or repurpose articles or portions of articles** can be obtained by following the guidelines here.

The following resources related to this article are available online at www.sciencemag.org (this infomation is current as of May 12, 2011):

**Updated information and services,** including high-resolution figures, can be found in the online version of this article at:

http://www.sciencemag.org/content/332/6031/828.full.html

Supporting Online Material can be found at:

http://www.sciencemag.org/content/suppl/2011/05/11/332.6031.828.DC1.html

This article appears in the following **subject collections**: Materials Science

http://www.sciencemag.org/cgi/collection/mat\_sci

capacitance between the top gate and the interface at the lowest measurement frequency. The negative current observed at low carrier densities reveals that the electric field penetrating through the metallic interface is negative, which arises from overscreening of the external field by the mobile electrons at the LAO/STO interface. Such a negative signal cannot be reconciled with any change of the dielectric properties of the LAO layer or the STO substrate. To further explore the electronic properties of the interface, we follow the analysis of (6), which has shown that for low frequencies f the penetration current  $I_{\gamma}$  goes as

$$I_{\rm v} = 2\pi f C_1 C_2 V_{\rm ac} / C_{\rm q} \tag{2}$$

where  $C_2$  is the geometric capacitance between the top gate and the interface and  $C_1$  is that between the back gate and the interface normalized by the area of the top gate. We measured  $C_1$  and  $C_2$  directly. For device 1,  $C_1$  = 4.67 pF,  $C_2$  = 1.1 nF, and  $V_{\rm ac}$  = 20 mV. For device 2,  $C_1$  = 14.3 pF,  $C_2$  = 4.01 nF, and  $V_{\rm ac}$  =10 mV. [For device 3, the penetration signal was small and difficult to resolve at 300 K because the STO dielectric constant decreases by three orders of magnitude (figs. S4 and S5)].

For device 1, at  $V_{\rm g} < -0.18$  V, the penetration current  $I_{\rm y}$  was no longer proportional to f, which might be attributed to the dc leakage in this region, although we do not know the precise mechanism by which a dc leakage would affect the measurement. The same deviation occurred with device 2 at positive  $V_{\rm g} > 0.37$  V. Thus, we excluded these regions in the analysis.

Using the penetration current data, we determined the quantum capacitance  $C_q$  and used Eq. 2 to compute  $d\mu/dn$ . Figure 4, A and B, shows the  $d\mu/dn(n)$  dependence of devices 1 and 2, respectively. The zero of density was not well defined because the measurement frequency at very small densities was not sufficiently low to charge the device fully. In a wide-density range,  $d\mu/dn$  stayed negative, which provides direct evidence of the negative compressibility of the interface electron system.

The observed enhancement of capacitance and negative compressibility exist in a disordered electron system. As shown in Fig. 4C, near depletion the sheet resistivity of the interfacial layer becomes much larger than the resistance quantum  $h/e^2$ . Thus, the electrons are localized at low densities, and the system is well outside the range of the free electron approximation (figs. S1 and S2).

The large capacitance enhancement that results from the negative compressibility offers a possible gating mechanism to switch transistors by using small gate voltages. This could diminish heating in future devices (15, 19, 20). We emphasize that the observed large enhancement of C is affected by the large geometric capacitance  $C_{\text{geom}}$ . Taking derivatives on both sides of Eq. 1, we get  $\delta C/C = C\delta C_g/C_g^2$ ; a device with

larger  $C_{\rm geom}$  per unit area will have a larger relative enhancement of the total capacitance. An interface capacitor device with a thinner LaAlO<sub>3</sub> layer may thus reveal an even larger capacitance enhancement at low carrier densities. As material quality improves, it is plausible that at low densities the effective gate-layer capacitance could increase to several times the geometric value. Transistors fashioned from the oxide interface or other systems with small carrier densities could then have an effectively very "high- $\kappa$ " electrode, allowing the creation of small transistors that switch at low voltages and minimal gate-to-channel leakage (20).

#### References and Notes

- B. I. Bello et al., Zh. Eksp. Teor. Fiz. 80, 1596 (1981)
   [Sov. Phys. ]ETP 53, 822 (1981)].
- B. Tanatar, D. M. Ceperley, *Phys. Rev. B* 39, 5005 (1989)
- S. V. Kravchenko, D. A. Rinberg, S. G. Semenchinsky,
   V. M. Pudalov, *Phys. Rev. B* 42, 3741 (1990).
- J. P. Eisenstein, L. N. Pfeiffer, K. W. West, *Phys. Rev. Lett.* 68, 674 (1992).
- J. P. Eisenstein, L. N. Pfeiffer, K. W. West, *Phys. Rev. B* 50, 1760 (1994).
- S. C. Dultz, H. W. Jiang, Phys. Rev. Lett. 84, 4689 (2000).
- 7. G. Allison *et al.*, *Phys. Rev. Lett.* **96**, 216407 (2006).
- 8. S. Shapira et al., Phys. Rev. Lett. 77, 3181 (1996).
- R. C. Ashoori, R. H. Silsbee, Solid State Commun. 81, 821 (1992).
- 10. A. Ohtomo, H. Y. Hwang, Nature 427, 423 (2004).

- S. Thiel, G. Hammerl, A. Schmehl, C. W. Schneider,
   Mannhart, Science 313, 1942 (2006).
- S. Okamoto, A. J. Millis, N. A. Spaldin, *Phys. Rev. Lett.* 97, 056802 (2006).
- 13. J. Mannhart, D. G. Schlom, Science 327, 1607 (2010).
- J. Mannhart, D. H. A. Blank, H. Y. Hwang, A. J. Millis,
   J.-M. Triscone, MRS Bull. 33, 1027 (2008).
- 15. T. Kopp, J. Mannhart, J. Appl. Phys. 106, 064504 (2009).
- 16. Materials and methods are available as supporting material on *Science* Online.
- 17. A. F. Edge *et al.*, *Appl. Phys. Lett.* **88**, 112907 (2006).
- K. A. Müller, H. Burkard, *Phys. Rev. B* 19, 3593 (1979).
   M. S. Loth, B. Skinner, B. I. Shklovskii, *Phys. Rev. E Stat.*
- Nonlin. Soft Matter Phys. **82**, 056102 (2010).

  20. P. M. Solomon, in Future Trends In Microelectronics:
  From Nanoparticles to Sensors and Energy, S. Luryi,
  J. M. Xu, A. Zaslavsky, Eds. (Wiley IEEE Press, Hoboken,
- NJ, 2010), pp. 127–140.

  21. The authors gratefully acknowledge helpful discussions and interactions with O. E. Dial, M. M. Fogler, R. Jany, P. A. Lee, L. S. Levitov, A. J. Millis, B. Shklovskii, P. Solomon, and J.-M. Triscone. This work was supported by ARO-54173PH, by the National Science Foundation through the Nanoscale Science and Engineering Center program, by the Deutsche Forschungsgemeinschaft (TRR 80), the European Commission (OxlDes), and by the Nanoscale Research Initiative. L. Li thanks the MIT Pappalardo Fellowships in Physics for support.

### Supporting Online Material

www.sciencemag.org/cgi/content/full/332/6031/825/DC1 Materials and Methods

SOM Text

Figs. S1 to S5

References

11 February 2011; accepted 28 March 2011

10.1126/science.1204168

# Beating Crystallization in Glass-Forming Metals by Millisecond Heating and Processing

William L. Johnson,\* Georg Kaltenboeck, Marios D. Demetriou, Joseph P. Schramm, Xiao Liu, Konrad Samwer, C. Paul Kim, Douglas C. Hofmann

The development of metal alloys that form glasses at modest cooling rates has stimulated broad scientific and technological interest. However, intervening crystallization of the liquid in even the most robust bulk metallic glass-formers is orders of magnitude faster than in many common polymers and silicate glass-forming liquids. Crystallization limits experimental studies of the undercooled liquid and hampers efforts to plastically process metallic glasses. We have developed a method to rapidly and uniformly heat a metallic glass at rates of 10<sup>6</sup> kelvin per second to temperatures spanning the undercooled liquid region. Liquid properties are subsequently measured on millisecond time scales at previously inaccessible temperatures under near-adiabatic conditions. Rapid thermoplastic forming of the undercooled liquid into complex net shapes is implemented under rheological conditions typically used in molding of plastics. By operating in the millisecond regime, we are able to "beat" the intervening crystallization and successfully process even marginal glass-forming alloys with very limited stability against crystallization that are not processable by conventional heating.

glass is formed when a liquid is undercooled below the melting point,  $T_{\rm M}$ , of the competing crystalline solid(s) and then freezes at a glass transition temperature,  $T_{\rm g}$ , without crystallizing. Undercooled liquids and glasses are metastable phases, implying that given sufficient time, both will transform to more stable crystalline solids. The glass-forming ability of a liquid is a measure of its metastability; that

is, its resistance to crystallization in the undercooled temperature region between  $T_{\rm g}$  and  $T_{\rm M}$ . Robust glass-forming silicate, polymer, and molecular melts exhibit superior metastability, with

Keck Laboratory of Engineering, California Institute of Technology, Pasadena, CA 91125, USA.

\*To whom correspondence should be addressed. E-mail: wlj@caltech.edu

crystallization time scales that range from minutes to hours, or longer, over the entire undercooled liquid region. Metallic glass formation was first reported by Klement et al. (1) in a eutectic Au-Si alloy that was rapidly quenched through the undercooled liquid region at a cooling rate of 10<sup>6</sup> K/s. At the time, this result was considered surprising because crystallization in undercooled metals and atomic liquids was presumed to be so rapid as to preclude glass formation altogether. Metal alloys with enhanced liquid metastabiity that form glass at substantially lower cooling rates (1 to 10<sup>3</sup> K/s), so-called bulk metallic glasses, were first developed in the early 1980s (2). Their development (2, 3) and the use of techniques to suppress the nucleation of crystals such as containerless processing (4, 5), fluxing (2), and preparation of high-purity alloys (6) led to improved metastability of metallic glass-forming melts. Nevertheless, the crystallization rates of these glass-forming metallic liquids remain orders of magnitude higher than those of common glassforming polymers, silicates, or molecular liquids. Consequently, experimental studies in undercooled metallic liquids are broadly limited by the intervening crystallization of the melt (7, 8). Measurements of thermodynamic functions, viscosity, atomic diffusion, and crystallization kinetics are generally restricted to temperatures just below  $T_{\rm M}$  or just above  $T_{\rm g}$  and are precluded at intermediate undercooling. For instance, viscosity data on metallic glass-forming melts are generally nonexistent for viscosities in the range from 10<sup>1</sup> to 10<sup>6</sup> Pa·s, because time scales for traditional rheometry exceed crystallization time scales. On the technology side, the application of net-shape thermoplastic forming processes such as injection molding (9, 10), blow molding (11), and microreplication (12-14) to fabricate high-performance, net-shape metal-glass hardware was met with limited success (15). For

polymer plastics, these technologies have been transformative due in large part to using relatively low process viscosities of 1 to 10<sup>4</sup> Pa·s (16). Implementation of these methods for metallic glasses has been restricted, however, because of high melt viscosities (>10<sup>6</sup> Pa·s) in the accessible temperature range near the glass transition.

To appreciate the difficulty of avoiding crystallization while processing a liquid at intermediate undercooling, consider the time scale required to relax spatial temperature variations within a sample by heat conduction. For a metallic glass of typical thermal diffusivity of  $\sim 10^{-2}$  cm<sup>2</sup>/s and sample dimensions of several millimeters, this time scale is typically 1 to 10 s. Several multiples of this time are required to establish a uniform temperature. Heating methods that supply heat through the sample boundary do not permit uniform heating in shorter times. To heat more rapidly requires that power be dissipated homogeneously and volumetrically throughout the sample so that temperature variations are never created. Ohmic dissipation by a uniform current density is one way to achieve this. In this work, we exploited the large and nearly temperature-independent electrical resistivity of metallic glasses (17, 18) and used an intense millisecond current pulse to achieve uniform ohmic heating from the glass to the undercooled liquid at rates of  $\sim 10^6$  K/s. We used highframe-rate video, thermal imaging, and high-speed infrared pyrometry to conduct millisecond timescale viscosity and dynamic enthalpy measurements in the undercooled liquid at temperatures where intervening crystallization precludes conventional rheometry and calorimetry, which are limited to much lower heating and cooling rates. We further demonstrated rapid millisecond injection molding of metallic glass rods into netshape metallic glass parts under liquid viscosity, pressure, and strain rate conditions widely established as optimum in plastic-forming technology.

the glass transition at  $T_g$  and onset of crystallization at  $T_x$  are heating rate-dependent, and the rate-dependent temperature interval,  $\Delta T =$  $T_x - T_g$ , defines an available process window for the undercooled liquid. Larger values of  $\Delta T$ indicate higher metastability of the liquid with respect to crystallization. Figure 1 illustrates the dependence of  $T_x$  and  $T_g$  on heating rate for the highly processable bulk metallic glass Vitreloy 1 ( $Zr_{41.2}Ti_{13.8}Cu_{12.5}Ni_{10}Be_{22.3}$ ). This alloy is a superior metallic glass-former, with a critical casting thickness of 3 to 4 cm. At a conventional heating rate of 20 K/min, one has  $T_g \approx 620$  K,  $T_x \approx 705 \text{ K}$ , and  $\Delta T \approx 85 \text{ K}$  (19). Above a critical heating rate of ~200 K/s, crystallization is avoided entirely during heating (20). This heating rate is roughly two orders of magnitude greater than the critical cooling rate of ~2 K/s (21) that is required to avoid crystallization during quenching of the liquid from high temperature to form the glass. Such heating and cooling rate asymmetry is observed for other systems [such as Pd<sub>43</sub>Ni<sub>10</sub>Cu<sub>27</sub>P<sub>20</sub> (22)] and is believed to be a general feature of the crystallization kinetics of a metallic glass. For comparison, a marginal glass-forming alloy (a metallic glass with critical casting thickness limited to few millimeters) will exhibit a crystallization curve as in Fig. 1 that is shifted to the left by about two orders of magnitude and thereby have a critical heating rate of ~10<sup>4</sup> K/s. As illustrated in Fig. 1, our novel approach permits heating at rates of ~10<sup>6</sup> K/s to a preselected liquid temperature and thereby enables access to temperatures shown in the upper left quadrant of Fig. 1 on time scales many orders of magnitude shorter than previously possible. The use of electrical current or current pulses

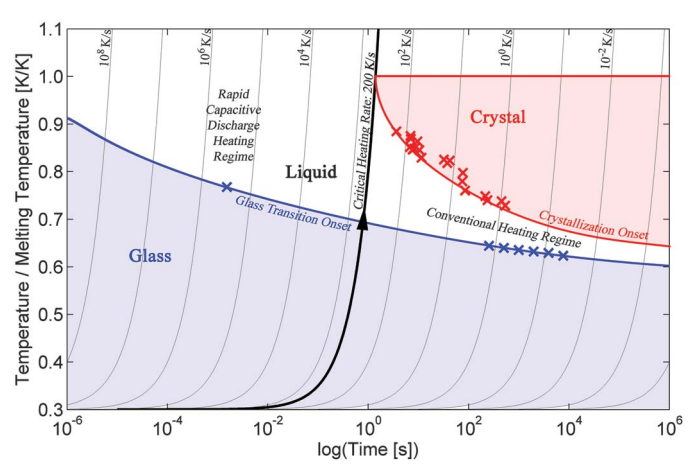
When a metallic glass is continuously heated,

and associated Joule heating to locally cut and shear metallic-glass ribbons was reported 20 years ago by Ballard et al. (23). In what could be viewed as a precursor to the present work, Gibbs et al. (24) and Zaluska, Kulik, and Matyja (25, 26) used ohmic heating to carry out rapid transient annealing of ferromagnetic metallicglass ribbons. Yavari and co-workers (27, 28) used a current-carrying tungsten electrode tip to locally heat and engrave surfaces, and performed joining-welding of rods by passing a large current density through the junction between the rods. In contrast, we focused on uniform volumetric heating of bulk samples to temperatures spanning the entire undercooled liquid region and on subsequent rapid characterization and processing of the undercooled melt.

The electrical resistivity  $\rho_e$  of metallic glasses and corresponding liquids is relatively large (~100 to 250  $\mu\Omega$ ·cm), exhibits a small and frequently negative temperature coefficient [|S| =  $|(1/\rho_e)d\rho_e/dT| \le 1 \times 10^{-4} \text{ K}^{-1}$ ] (17, 18), and varies smoothly and continuously as the glass transition at  $T_g$  is traversed. Crystalline metals and alloys have much smaller resistivity (typically 1 to 50  $\mu\Omega$ ·cm), a larger and positive temperature coefficient ( $S \sim 10^{-2}$  to  $10^{-4}$  K<sup>-1</sup>), and

Fig. 1. Glass-transition onset temperature and crystallization onset temperature versus time for the metallic glass Vitreloy 1 at varying heating rates. Glass transition data are taken from Wang et al. (19) and crystallization data from Schroers et al. (20). The critical heating rate to completely bypass crystallization on heating from the glass through the liquid is about 200 K/s (20). Conventional heating

rates on the order of 1 K/s



provide access to the undercooled liquid over a rather narrow temperature range, above which crystal-lization becomes kinetically favorable. Using the present approach, which enables heating rates on the order of  $10^6$  K/s, the undercooled liquid is accessible at any temperature above the glass transition, through the melting point and beyond, where the liquid enters the equilibrium state (upper left quadrant in the diagram). The glass transition data point plotted in this regime was obtained in the present study under a heating rate of  $\sim 3 \times 10^5$  K/s (Fig. 3B).

large discontinuous jump in resistivity on melting. Under high imposed current densities and ohmic dissipation, the heating of crystalline metals tends to spatially localize. Local resistivity and temperature variations (at contacts, interfaces, or inhomogeneities) along the direction of current flow are amplified by increased dissipation in hotter regions. This results in a runaway melting instability as observed, for example, in capacitive discharge welding of metals, in which melting spatially localizes at interfaces, contacts, and areas of high initial resistance. Heating localization in metallic glasses is mitigated by their small |S| and by the absence of a melting discontinuity. A discussion of the requirements for rapid uniform ohmic heating and their application to metallic glasses is provided in the supporting online material (SOM).

In the present work, a capacitor bank with capacitance C = 0.264 F and charging voltage up to  $V_0 = 200$  V was used to store energies up to  $E = CV_0^2/2 = 5280$  J. The discharge circuit used was a series RLC circuit tuned to near the critical damping condition that permits a maximum rate of energy dissipation with no circuit ringing or overshoot. For the critically damped circuit, the characteristic time constant for the discharge and dissipation of electrical energy is  $\tau_h \approx 0.4$  ms. See the SOM for details of the RLC circuit and its time response.

Vitreloy 1 rods 4 mm in diameter and 2 cm in length were uniformly heated by capacitive discharge coupled through copper electrodes. The rod was heated from ambient temperature to processing temperatures between  $T_{\rm g}$  and  $T_{\rm M}$  in about 1 ms. After heating, the rod was deformed under a compressive force of ~400 N applied via the electrodes. Figure 2 shows infrared images (20,480 pixels) of the central portion of a rod at 0.75-ms intervals during heating to a final average temperature of 799 K. This final temperature,  $T_{\rm F}$ , is ~180 K above the reported  $T_{\rm g}$  measured by conventional calorimetry (Fig. 1) at a heating rate of 20 K/min. The sample geometry used is shown in Fig. 3A. The center column of Fig. 2 shows the temperature profile measured by the row of pixels located along the rod's vertical centerline. The distribution of temperatures measured by all pixels is shown in the right column of Fig. 2. The half width at half maximum of final temperature distribution (right column of Fig. 2) was ~3.5 K. The low-temperature tail observed in the overall distribution is caused by edge effects visible in the thermal images. Although thermal imaging measures surface temperature, an analysis of dynamic electric field penetration effects by Lohöfer and Pottlacher (29) (see the SOM for more details) shows that temperature inhomogeneity along the radial direction in the rod interior should be less than 1% of the total heating interval, or less than 5 K, with the rod centerline expected to be slightly cooler than the surface. The overall temperature distribution of the heated metallic glass rod is remarkably uniform.

After heating, deformation under the applied load began at an elapsed time of about 3 ms and continued to about 8 ms (Figs. 2 and 3B). The average temperature rose by about 10 to 15 K during compressive deformation of the rod. This delayed rise is attributed to dissipation of the mechanical work performed by the piston during deformation. Beyond 10 ms, the deformed

sample began to cool by radiative and conductive heat loss to the surroundings. Cooling, however, becomes significant only on time scales of several tenths of a second—considerably longer than the time scales for which the present data are analyzed.

To observe detailed transient features of the heating history, an ultrafast infrared pyrometer

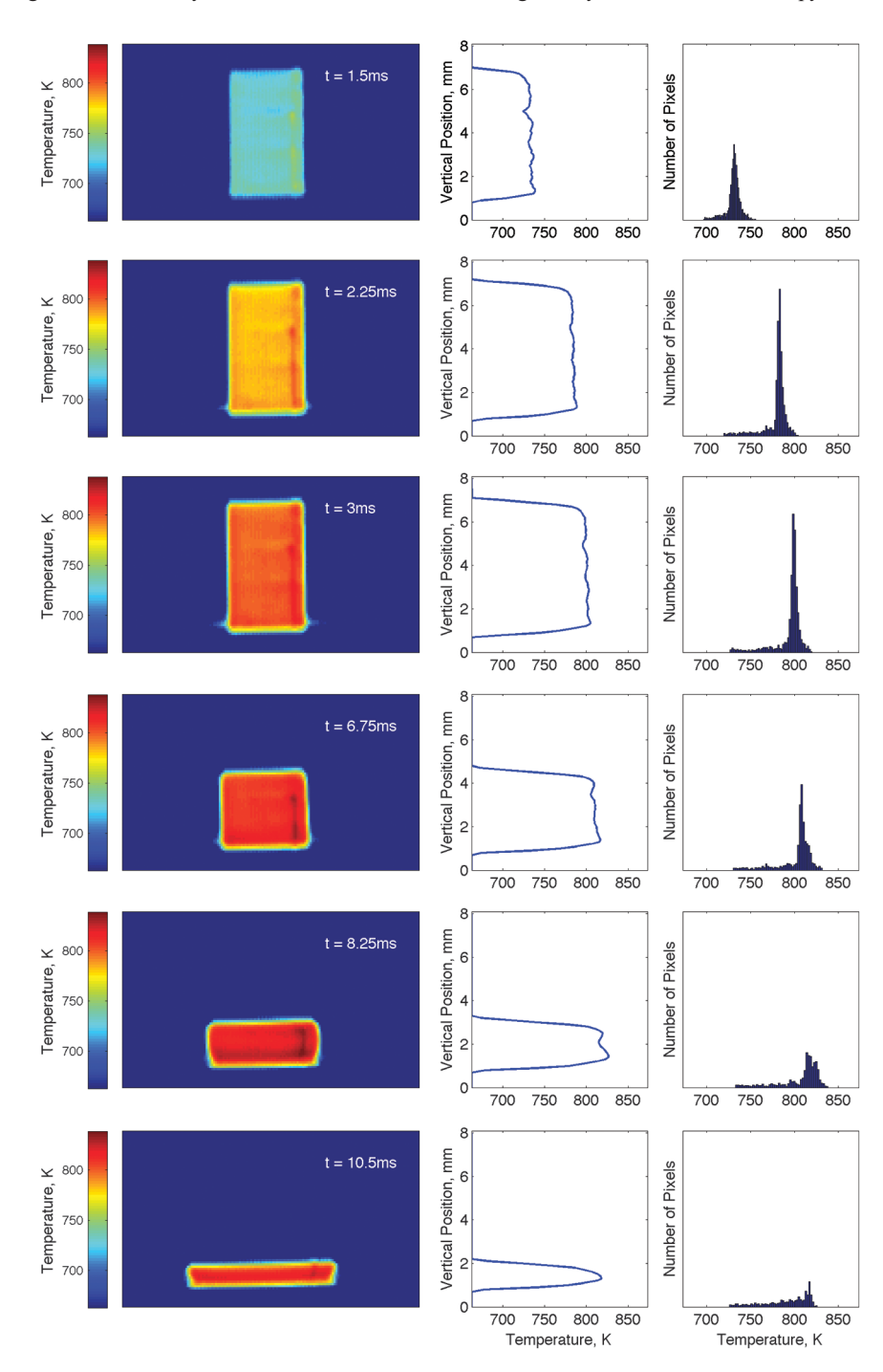


**Fig. 2.** Thermal imaging during capacitive discharge heating. (**Left column**) Selected frames taken from an infrared imaging camera movie; (**middle column**) temperature measured by pixels along the vertical centerline of the rod; (**right column**) histogram of temperature measured by all pixels in the image. The half width at half maximum of final temperature distribution (right column) is ~3.5 K. The low-temperature tail observed in the overall distribution is caused by edge effects that are visible in the thermal images.

with time resolution of 5 µs (SOM) was used to track temperature with much higher time resolution. The high-resolution heating curve of a separate Vitreloy 1 sample is shown in red in the inset of Fig. 3B. The dimensions and heating parameters of this sample were identical to the one discussed above, but it was heated in the absence of an applied force so that no viscous deformation occurs. A dynamic glass transition at ~775 K was observed, as revealed by a large horizontal step in the time-temperature trace. The step corresponds to an endothermic heat absorption. At the applied heating rate of  $\sim$ 3 ×  $10^{5}$  K/s, the  $T_g$  was shifted by ~155 K above that observed by conventional calorimetry (620 K at a much lower heating rate of 0.67 K/s; Fig. 1). After the glass transition, temperature stabilized at a steady plateau value for several milliseconds, indicating that the final heated liquid lost negligible heat to the surroundings for the duration of the plateau. Measurements performed in this plateau regime will therefore be essentially adiabatic. We fitted the high-resolution heating curve below  $T_{\rm g}$  to the analytic solution for dissipation of power by the RLC circuit, given by  $T(t) - T_0 \sim \int_0^t t^2 \exp(-t/\tau_h) dt$ , to estimate the heating time constant  $\tau_h \approx 0.33$  ms (SOM). The discrepancy between the final steady-state tem-

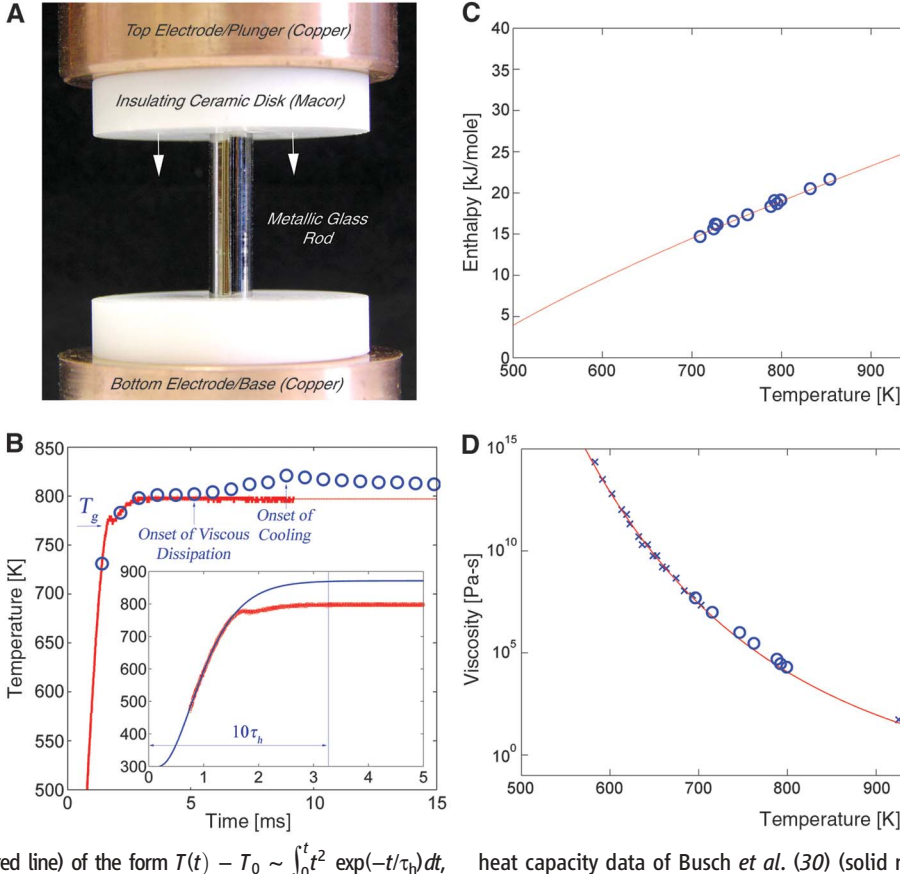
perature predicted by the fit and that measured by the pyrometer is attributed to the enthalpy absorption associated with the dynamic transition from an overheated glass to the equilibrium liquid, commonly referred to as enthalpy recovery. The rapid pyrometry with microsecond time resolution, together with the known transient power dissipation, permits enthalpy versus temperature measurements at very high heating rates. The system is effectively a scanning calorimeter operating at scanning rates of 105 to 106 K/s. As discussed earlier, this is enabled by the uniform ohmic dissipation of heat, whereby temperature gradients are never created. In conventional calorimetry, heat is supplied from the sample boundaries, and scanning rates are limited by thermal relaxation times on the order of 1 to 10 s.

Figure 3C summarizes relevant data on the total specific energy dissipated in the rod, h, and average final sample temperature  $T_{\rm F}$ , for numerous experiments. The specific enthalpy per mole,  $h = (\varepsilon M/2m)CV^2$  (*m* is sample mass, and M is the average atomic weight), dissipated in the rod is the total energy stored in the capacitor corrected by an efficiency factor,  $\varepsilon = R_s/(R_s + R_0)$ , where  $R_s$  is the sample resistance, and  $R_0$  is the resistance of the circuit with no sample (SOM). The  $h(T_{\rm F})$  data collected from a number of ex-

periments are plotted in Fig. 3C to obtain a complete h(T) relation for liquid Vitreloy 1 over the undercooled liquid region between 700 and 900 K, previously inaccessible. This h(T) relation is for a configurationally relaxed liquid (as opposed to an overheated glass). Using conventional calorimetry, Busch et al. (30) reported the experimental heat capacity  $(c_P)$  of Vitreloy 1 for both the glassy and liquid states up to about 700 K and for the high-temperature liquid near  $T_{\rm M}$  down to about 900 K. For the liquid, they fitted their data to interpolate  $c_P(T)$  over the undercooled liquid region using a standard functional form  $c_P = 3R + 7.50 \times 10^{-3} T + 8.17 \times$  $10^6 T^2$  (J/mol K), where first two terms in this equation describe the glass below  $T_{\rm g}$  (R is the gas constant). Integrating this expression gives a predicted specific enthalpy h(T) curve that is compared with the present h(T) data plotted in Fig. 3C. The comparison shows excellent agreement.

During dynamic deformation, the timedependent height of the deforming rod, y(t), was measured using frame-by-frame video images. The digitized data were fitted to an analytic functional form that can be differentiated to determine the velocity, dy/dt, and acceleration,  $d^2y/dt^2$ , of the pneumatic drive assembly during defor-

Fig. 3. Thermodynamic and rheological measurements using capacitive discharge heating. (A) Experimental setup used to measure enthalpy and viscosity. The metallic glass rod is inset into ceramic disks making contact with copper electrodes. (B) (Solid red curve) Thermal trace of an undeformed Vitreloy 1 rod as recorded by a single-pixel high-framerate infrared pyrometer. The onset of  $T_{q}$  at 770 K is indicated. (Blue circles) Temperature response of a deforming Vitreloy 1 rod versus time (same dimensions and conditions as above), averaged over multiple pixels as recorded by an infrared thermal imaging camera. The onset of viscous dissipation caused by deformation and the onset of cooling caused by heat loss to the surroundings are indicated. The inset shows a fit (thin blue line)



to the thermal trace (thick red line) of the form  $T(t) - T_0 \sim \int_0^t t^2 \exp(-t/\tau_h) dt$ , predicted for a critically damped RLC circuit (SOM). The fitting formula does not account for the enthalpy absorbed at  $T_{\alpha}$  and consequently overshoots the measured thermal response. (C) Experimental enthalpy  $h = (\varepsilon/2)$  $CV^2$  versus temperature  $T_F$  (blue circles) and enthalpy computed from liquid

heat capacity data of Busch et al. (30) (solid red curve) for Vitreloy 1. (D) Viscosity versus temperature for Vitreloy 1 measured using capacitive discharge heating (blue circles) compared with viscosity data reported in the literature (blue crosses) using beam bending, parallel plate rheometry, and Couette viscometry (34).

900

1000

1100

900

1000

1100

1200

1200



**Fig. 4.** Experimental setup based on the capacitive discharge heating approach used to demonstrate injection molding of a metallic glass component. (**A**) Basic setup comprising an upper copper electrode used as a plunger, a lower copper electrode used as a base (not shown), and a quartz sleeve used as an insulating barrel to electrically insulate and confine the sample charge. A groove is introduced in the quartz sleeve at the point of contact with the mold runner to enable entry of the softened glass into the mold (not shown). (**B**) A simple "as-molded"  $Pd_{43}Cu_{27}Ni_{10}P_{20}$  toroidal metallic glass part formed at a processing temperature of ~720 K using a plunger pressure of ~20 MPa. The sample is free of visible flow defects, and no oxidation can be detected despite being processed in open air. (**C**) Lower half of the mold tool used to mold the metallic glass component.

mation. These data were used to compute strain rate versus time, and with knowledge of the applied force, the viscosity  $\eta$  at  $T_F$ . Because the sample temperature increases slightly during deformation (Fig. 3B), the viscosity is measured over a slightly increasing temperature interval. As explained in the SOM, the limited force available (400 N) and response time of the drive system (inertial effects) make the present setup most suitable for measuring viscosities in the range from 10<sup>4</sup> to 10<sup>7</sup> Pa·s. Radiative heat loss from the rod surface to the surroundings, and heat loss by conduction to the ceramic plates and cold electrodes (located several millimeters behind the ceramic surface), can be neglected in the deforming region on the time scale of the experiment (typically 5 to 15 ms). In other words, the viscosity measurements are carried out under essentially adiabatic conditions. Using the relation  $\eta = Fy^2/[3v_0(dy/dt)]$  (31), appropriate to the early stage of deformation (SOM), where F is the applied force and  $v_0$  the sample volume, the viscosity was determined from a number of experiments at various  $T_{\rm F}$ 's. In Fig. 3D, the results are compared with previously reported viscosity data on Vitreloy 1 obtained with conventional rheology. Conventional beam-bending and parallel plate rheometry (32, 33) require time scales of at least tens of seconds, which limits data to about 80 K above  $T_g$ . Couette viscometry (34) at higher temperature (and lower viscosities) similarly requires time scales of at least tens of seconds and is precluded by the intervention of crystallization at temperatures below ~900 K.

The ability to dynamically process metallic glasses at any undercooled liquid temperature on millisecond time scales creates the opportunity to carry out rapid thermoplastic forming at far lower process viscosities and pressures than was previously possible. Commercial injection molding of plastics is carried out at typical temperatures of 450 to 700 K, process viscosities of 1 to 10<sup>4</sup> Pa·s, and injection pressures of 1 to 30 MPa (16). To demonstrate injection molding of bulk metallic glasses using typical plastic molding conditions, we designed and constructed a simple injection-molding apparatus. The basic elements of the setup are shown in Fig. 4A. Several variants of this apparatus were used to injection-mold net-shape components from Vitreloy 1 and Pd<sub>43</sub>Ni<sub>10</sub>Cu<sub>27</sub>P<sub>20</sub>. Figure 4B shows a net-shape metallic glass component with semicircular toroidal geometry molded from a glassy rod of Pd<sub>43</sub>Cu<sub>10</sub>Ni<sub>27</sub>P<sub>20</sub>. Figure 4C shows the upper mold tool used to produce the component. The part was produced by rapid heating at  $10^6$  K/s to  $T_F \approx 720$  K, followed by injection into the mold cavity with an applied pressure of ~20 MPa. The processing viscosity of the Pd43Ni10Cu27P20 melt at 720 K is estimated to be  $\sim 10^3$  Pa·s (35). The total time required to form this component was about 40 ms, as determined by monitoring the displacement of the electrode/plunger using high-speed video. This implies strain rates on the order of  $10^3$  to 10<sup>4</sup> s<sup>-1</sup> during the molding process. The rheological conditions (viscosity, pressure, and strain rate) are typical of those used in commercial injection molding of plastic hardware (16). X-ray diffraction and differential scanning calorimetry show that the product parts are fully glassy for both the Vitreloy 1 and the Pd<sub>43</sub>Cu<sub>10</sub>Ni<sub>27</sub>P<sub>20</sub> alloy. This is expected because the processing times are much shorter than the time for intervening crystallization (as seen in Fig. 1). Moreover, no visible oxidation was detected in either of the parts, despite being processed in open air.

Concerning intervening crystallization, it is of obvious interest to explore the applicability of our rapid heating and forming methods to less robust, or marginal, metallic glass-formers, such as those with critical casting thicknesses of several millimeters (as opposed to several centimeters). As discussed earlier, marginal glass-formers have crystallization curves shifted to time scales about two orders of magnitude shorter than the robust glass-formers Vitreloy 1 and Pd<sub>43</sub>Cu<sub>10</sub>Ni<sub>27</sub>P<sub>20</sub> (Fig. 1). The marginal metallic glass-forming alloy Zr<sub>11</sub>Ti<sub>33</sub>Cu<sub>47</sub>Ni<sub>8</sub>Si<sub>1</sub> (36) has a critical casting rod diameter of 5 to 6 mm and exhibits a very restricted processing window  $\Delta T \approx 50$  K at conventional heating rates. Thus, its crystallization curve is shifted not only to shorter times but also to lower temperatures closer to  $T_{\rm g}$  (Fig. 1). Fully glassy sample rods 3 mm in diameter and 2 cm long were prepared and heated by rapid discharge at  $\sim 10^6$  K/s to temperatures midway between  $T_g$  and  $T_M$ . The rods were deformed under a compressive load of ~400 N between copper electrode plates (as in Fig. 3A) but without ceramic spacers. The rods were heated and deformed to flat uniform disks of final thicknesses ranging from 0.5 to 1 mm in total elapsed times of less than 30 ms. The deforming samples were effectively quenched between the copper electrode plates. X-ray diffraction and differential scanning calorimetry verified that the deformed disks were fully glassy, thereby demonstrating that crystallization was avoided in this marginal glass-former.

The rapid uniform heating approach introduced here allows access to metastable undercooled liquid states of intermediate mobility at temperatures and time scales far outside those probed by traditional methods. This platform enhances the experimental study of thermophysical properties, flow behavior, relaxation phenomena, and crystallization kinetics of undercooled metallic liquids. For example, it enables scanning calorimetry at heating rates of  $\sim 10^6$  K/s. On the technology side, the method circumvents intervening crystallization and enables thermoplastic processing and forming of robust as well as marginal glassforming alloys over the entire range of viscosity observed in undercooled metallic glass-forming melts.

### **References and Notes**

- W. Klement, R. H. Willens, P. Duwez, *Nature* 187, 869 (1960)
- H. W. Kui, A. L. Greer, D. Turnbull, Appl. Phys. Lett. 45, 615 (1984).
- 3. A. Peker, W. L. Johnson, Appl. Phys. Lett. 63, 2342 (1993).
- 4. D. M. Herlach, R. F. Cochrane, I. Egry, H. J. Fecht,
  - A. L. Greer, Int. Mater. Rev. 38, 273 (1993).

- 5. Y. J. Kim, R. Busch, W. L. Johnson, A. J. Rulison, W. K. Rhim, Appl. Phys. Lett. 65, 2136 (1994).
- 6. X. H. Lin, W. L. Johnson, W. K. Rhim, Mater. Trans. Jpn. Inst. Metals 38, 473 (1997).
- 7. W. L. Johnson, MRS Bull. 24, 42 (1999).
- 8. A. Inoue, Acta Mater. 48, 279 (2000).
- 9. G. Duan et al., Adv. Mater. (Deerfield Beach Fla.) 19, 4272 (2007).
- 10. A. Wiest, J. S. Harmon, M. D. Demetriou, R. D. Conner, W. L. Johnson, Scr. Mater. 60, 160 (2009).
- 11. J. Schroers, Q. Pham, A. Peker, N. Paton, R. V. Curtis, Scr. Mater. 57, 341 (2007).
- 12. Y. Saotome, Y. Noguchi, T. Zhang, A. Inoue, Mater. Sci. Eng. A 375-377, 389 (2004).
- 13. G. Kumar, H. X. Tang, J. Schroers, Nature 457, 868
- 14. G. Kumar, A. Desai, J. Schroers, Adv. Mater. (Deerfield Beach Fla.) 23, 461 (2010).
- 15. J. Schroers, Adv. Mater. (Deerfield Beach Fla.) 22, 1566
- 16. C. D. Han, Rheology and Processing of Polymeric Materials: Polymer Processing (Oxford Univ. Press, Oxford, 2007).
- 17. H. J. Güntherodt, Adv. Solid State Phys. 17, 25 (1977).
- 18. S. R. Nagel, Phys. Rev. B 16, 1694 (1977).

- 19. W. H. Wang, L. L. Li, M. X. Pan, R. J. Wang, Phys. Rev. B 63, 052204 (2001).
- 20. J. Schroers, A. Masuhr, W. L. Johnson, R. Busch, Phys. Rev. B 60, 11855 (1999).
- 21. Y. J. Kim, R. Busch, W. L. Johnson, A. J. Rulison, W. K. Rhim, Appl. Phys. Lett. 68, 1057 (1996).
- 22. J. Schroers, W. L. Johnson, R. Busch, Appl. Phys. Lett. 77, 1158 (2000).
- D. E. Ballard, P. G. Frischmann, A. I. Taub, U.S. Patent 5,005,456 (1991).
- 24. M. R. I. Gibbs, D. H. Lee, I. E. Evetts, IEEE Trans, Maan,
- 20. 1373 (1984). 25. A. Zaluska, H. Matyja, Int. J. Rapid Solidif. 2, 205 (1986).
- 26. T. Kulik, H. Matyja, Mater. Sci. Eng. A 133, 232 (1991).
- 27. M. F. de Oliveira, W. J. Botta, C. S. Kiminami, A. Inoue, A. R. Yavari, Appl. Phys. Lett. 81, 1606 (2002).
- 28. A. R. Yavari, M. F. de Oliveira, C. S. Kiminami, A. Inoue, W. J. F. Botta, Mater. Sci. Eng. A 375-377, 227
- 29. G. Lohöfer, G. Pottlacher, Int. J. Thermophys. 26, 1239
- 30. R. Busch, Y. J. Kim, W. L. Johnson, J. Appl. Phys. 77, 4039 (1995)
- 31. J. Lu, G. Ravichandran, W. L. Johnson, Acta Mater. 51,

- 32. G. J. Dienes, H. F. Klemm, J. Appl. Phys. 17, 458 (1946).
- 33. T. A. Waniuk, R. Busch, A. Masuhr, W. L. Johnson, Acta Mater. 46, 5229 (1998).
- 34. A. Masuhr, T. A. Waniuk, R. Busch, W. L. Johnson, Phys. Rev. Lett. 82, 2290 (1999).
- 35. G. J. Fan, H.-J. Fecht, E. J. Lavernia, Appl. Phys. Lett. 84, 487 (2004)
- 36. H. Choi-Yim, R. Busch, W. L. Johnson, J. Appl. Phys. 83, 7993 (1998).
- Acknowledgments: The authors acknowledge partial support by the II-VI Foundation, the assistance of R. Overstreet with the thermal imaging unit, and useful discussions with M. A. Nicolet. A patent filed by the California Institute of Technology is currently pending. The U.S. patent application number is US2009/0236017 A1.

### Supporting Online Material

www.sciencemag.org/cgi/content/full/332/6031/828/DC1 Materials and Methods Figs S1 and S2 References

We describe here a technique for 3D orientation mapping in the TEM (3D-OMiTEM) with

7 December 2010; accepted 1 April 2011 10.1126/science.1201362

## **Three-Dimensional Orientation Mapping in the Transmission Electron Microscope**

H. H. Liu, S. Schmidt, H. F. Poulsen, A. Godfrey, Z. Q. Liu, J. A. Sharon, X. Huang 1,5\*

Over the past decade, efforts have been made to develop nondestructive techniques for three-dimensional (3D) grain-orientation mapping in crystalline materials. 3D x-ray diffraction microscopy and differential-aperture x-ray microscopy can now be used to generate 3D orientation maps with a spatial resolution of 200 nanometers (nm). We describe here a nondestructive technique that enables 3D orientation mapping in the transmission electron microscope of mono- and multiphase nanocrystalline materials with a spatial resolution reaching 1 nm. We demonstrate the technique by an experimental study of a nanocrystalline aluminum sample and use simulations to validate the principles involved.

any materials are polycrystalline, meaning that they are composed of a large **▲**number of grains (crystallites) of different crystallographic orientations. A full threedimensional (3D) orientation mapping of such polycrystalline grain structures (with information about the position, size, morphology, and orientation of each grain, as well as the topological connectivity between the grains) is needed to re-

can be obtained with the 3D electron backscatter diffraction technique (3D-EBSD) (1). This technique has a spatial resolution of ~20 nm, but it requires serial sectioning of the sample as part of the data collection process and, thus, is destructive. Recently, two nondestructive 3D x-ray techniques that have a spatial resolution of, at best, 200 nm (2, 3) have been demonstrated. Electron tomography has been used to determine the shape of isolated crystals with a resolution down to 1 nm, but this method cannot be used to obtain orientation maps (4). Furthermore, several approaches (5-10) have been developed for 2D orientation mapping in the transmission electron microscope (TEM). In these approaches, the crystal orientation is determined from diffraction patterns that are either recorded directly using the diffraction mode (5-7) or reconstructed indirectly from conical-scanning dark-field images (8-10). These 2D methods are relevant when the specimen thickness is smaller than the size

late the structure to properties. Such information of the grains.

a spatial resolution on the order of 1 nm for specimens that may be substantially thicker than the average grain size. Similar to some of the 2D techniques (8-10), the data collection is based on conical-scanning dark-field imaging. However, to enable the simultaneous reconstruction of a complete 3D orientation map of all grains in a sample volume, images are recorded at many sample tilt angles. Furthermore, we have developed a new approach for the orientation determination and 3D reconstruction, based on the GrainSweeper (11) and GrainSpotter (12) algorithms originally developed for 3D reconstruction of synchrotron diffraction data. In this approach, the orientation of each voxel in the sample is determined by a simultaneous analysis of all contributing diffraction vectors derived from the dark-field images over all beam and sample tilt positions, thereby reducing the effects caused by dynamical diffraction and multiple scattering. A volume formed by adjacent voxels of the same orientation is identified as a grain. The shape and location of each grain are determined with the use of a ray-tracing method based on the sample tilt angles where the grain is visible in the dark-field images. The angular resolution for the orientation mapping is primarily determined by the step sizes used for the conical scanning and the sample tilting, whereas the spatial resolution is also determined by the magnification used to record the images. In general, however, more than 100,000 images are required to obtain nanoscale orienta-

To validate the principles of all procedures involved in the data analysis, we used a software package that incorporates dynamical diffraction and multiple scattering effects (13) to simulate electron diffraction from overlapping grains of different orientations. This package was used in combination with a 3D grain-orientation map

<sup>1</sup>Center for Fundamental Research: Metal Structures in Four Dimensions, Materials Research Division, Risø National Laboratory for Sustainable Energy, Technical University of Denmark, DK-4000 Roskilde, Denmark. <sup>2</sup>Laboratory of Advanced Materials, Department of Materials Science and Engineering, Tsinghua University, 100084 Beijing, P.R. China. <sup>3</sup>Shenyang National Laboratory for Materials Science, Institute of Metal Research, Chinese Academy of Sciences, 110016 Shenyang, P.R. China. <sup>4</sup>Department of Mechanical Engineering, Johns Hopkins University, Baltimore, MD 21218, USA. 5Danish-Chinese Center for Nanometals, Materials Research Division, Risø National Laboratory for Sustainable Energy, Technical University of Denmark, DK-4000 Roskilde, Denmark

\*To whom correspondence should be addressed. E-mail: xihu@risoe.dtu.dk